Fully-Connected Continuous Conditional Random Field With Stochastic Cliques for Dark-spot Detection In SAR Imagery

Linlin Xu, *Member, IEEE*, Mohammad Javad Shafiee,
Alexander Wong, *Member, IEEE*, David A. Clausi, *Senior Member, IEEE*

***Abstract*—Dark-spot detection from synthetic aperture radar (SAR) imagery is a fundamental step in marine oil-spill detection and monitoring. However, to achieve robust and accurate detection is difficult due to SAR sensor limitations and the complex marine environment. To address this problem, the large-scale spatial-contextual information in SAR imagery has to be utilized to increase the class separability between the dark-spot and the background. A stochastic fully-connected continuous conditional random field (SFCCRF) approach to model SAR imagery and perform soft-label inference has been designed and built, leading to an efficient detection algorithm. Instead of treating all pixels in the imagery as being connected, SFCCRF determines the connectivity of two pixels in a stochastic manner based on their proximity in both feature space and image space. Since SFCCRF provides an efficient and effective way for modeling the large-scale spatial correlation effect, the resulting soft-labels can resist the influence of speckle noise and highlight the difference between dark-spot and the background. Dark-spot detection is achieved by binarizing the soft-labels estimated by SFCCRF. The proposed algorithm is tested on both simulated and real SAR imagery. The results show that SFCCRF can delineate the dark-spot with low commission and omission error rates.**

I. Introduction

The operational discharge of oil from ships into the oceans is an ongoing global problem that greatly affects the marine and coastal environments [1]. Ships regularly produce oily bilge wastes which are often illegally discharged to avoid costly disposal fees at port. The total estimated volume of oil released from illegal "operational" discharges is more than that from large accidents [1], [2]. The presence of oil spills pollutes the sea water, destroys wildlife habitat and breeding grounds, and damages beaches, causing many social and environmental problems [1]–[3].

Advances in remote sensing technologies provide effective ways for oil spill monitoring to support the enforcement and cleanup efforts. In particular, the spaceborne synthetic aperture radar (SAR) remote sensing technique, due to its wide coverage, all-weather and all-day capability, has been widely used for oil spill monitoring. Current SAR sensors for oil-spill monitoring include RADARSAT-2, TerraSAR-X and Sentinel-1A [4]. Both the true oil spills and some "look-alike" phenomena (e.g., the low wind area, biogenic slicks and wave front) appear as dark-spots in SAR images because they can dampen short-capillary waves which are the main agent of SAR ocean backscattering [5]–[8].

Dark-spot detection from SAR imagery is a significant step in SAR oil spill monitoring. The objective of dark-spot detection is to identify all dark-formations in SAR imagery that are caused by either the true oil spills or the look-alikes. This step is important because the further classification of the true oil spills and the look-alikes has to be based on the detection results. Therefore, the detection accuracy in this step directly influence the ability of the monitoring system to identify the true oil spills. For example, unless a true oil spill can be detected at this dark-spot detection step, it can never be detected at a later step [9]. Moreover, accurate delineation of the boundaries of dark-spots/targets in the dark-spot detection step is crucial for extracting meaningful features to support the classification step.

This paper therefore focuses on dark-spot detection from SAR imagery. However, designing a robust and accurate detection algorithm is a challenging task due to the difficulties caused by the sensor limitations, the complex marine environment, as well as the characteristics of the true oil spills. First, dark-spot detection is affected by SAR sensor noise. SAR speckle is an inherent and deterministic part of SAR signal, and may provide useful information in some specific applications. However, SAR speckle is treated as noise due to its undesirable nature in the dark-spot detection task. The presence of speckle in SAR imagery will reduce the class separability between the targets and the background, and increase the difficulties to detect the targets. Note that besides the speckle noise, other noise, e.g., the sensor thermal noise, may also contribute to the noise-like patterns in the image. Second, the intensity contrast between the targets and the background could be too low for the targets to be detected as the ocean backscattering decreases, depending on the local sea state, incidence angle and spatial resolution of SAR imagery [3]. Third, the detection algorithm should have very high true positive rate to reduce the omission of true oil spill detections. However, the ship-generated spills tend to be very small in size and have thin and elongated geometric characteristics, which make them highly susceptible to the sensor and the complex marine environment.

Several methods have been proposed for dark-spot detection. Intensity thresholding is the commonly used approach for detecting dark-spot [10]–[14]. To resist speckle noise and increase the class separability, Shu et al. proposed a thresholding method that takes advantage of spatial density information [9]. Some researchers exploit the edge information in SAR image for dark-spot detection [15]–[18]. A neural network model has been used for joint dark-spot detection

and classification of oil spills [19]. Another neural network model [20] adopts the Weibull multiplicative filter to suppress speckle noise and enhance the contrast between the targets and the background, and the Multi-Layer Perceptron (MLP) neural networks to segment the filtered SAR image. The marked point process based approach [21] models the dark-spots by the marked point process under the Bayesian framework and adopts the Markov Chain Monte Carlo (MCMC) method to infer the class labels.

Although the thresholding-based approaches are fast for processing large images, they are very sensitive to SAR speckle noise. An effective thresholding approach relies on some spatial feature extraction techniques that are capable of resisting the influence of speckle noise, while highlighting differences between the target and background. If a clean image with distinguishing features can be obtained, applying the thresholding method to identify the dark-spots will be a straightforward task. Such an image can be achieved by some noise-suppression/denoising methods [22], which typically would smooth the image by conducting some spatial averaging operations [23]–[25]. Since the ship-generated targets generally have small, thin and elongated shapes, they are particularly sensitive to the denoising methods, which tend to easily erase the thin part of the targets and break the elongated targets. Therefore, an appropriate denoising method should not only suppress the speckle noise, but also preserve the details. Since image denoising essentially exploits the spatial correlation effect in the image, designing a desirable denoising method calls for an advanced spatial modeling approach that is capable of effectively and efficiently accounting for spatial correlation effect in SAR imagery.

II. Our Approach

In this paper, we develop a stochastic fully-connected continuous conditional random field (SFCCRF) approach to model SAR oil spill imagery and perform soft-label inference, leading to an efficient detection algorithm. A small value of the soft-label in SFCCRF indicates higher probability of being the target, but lower possibility of being the background. The soft-label is therefore equivalent to the "true" backscattering intensity for which a smaller value also indicates higher possibility of being the target. Since SFCCRF provides an efficient and effective way for modeling the large-scale spatial correlation effect, the resulting soft-labels can resist the influence of speckle noise and highlight the difference between the target and the background. To achieve the purpose of detection, a thresholding is performed on the soft-labels to obtain the binary labels.

The CRF model has been widely used for performing label inference in the computer vision literature [26], [27]. However, the ordinary CRF only accounts for the spatial correlation effect among pixels in a small neighborhood. Fully-connected CRF (FCRF) enhances CRF by addressing the correlation effect in global image scale, but at the cost of high computation. The proposed SFCCRF model maintains the advantages of FCRF but reduces it's computational cost by utilizing stochastic cliques [28]. SFCCRF follows the general framework for building the stochastic cliques in CRF, but adopts new features to address the particularity of SAR imagery for dark-spot detection.

In our previous publication [29], we proposed a TGSFCRF model, and demonstrated that modeling large-scale spatial correlation effect using the stochastic clique approach can capture useful spatial contextual information for enhancing detectability of targets. In this paper, we extend our previous work by proposing a SFCCRF algorithm which adopts the continuous CRF (CCRF) approach that yields continuous soft-labels [30], [31] rather than the traditional CRF model that produces discrete labels. The advantage of SFCCRF over TGSFCRF can be illustrated from the following aspects. First, TGSFCRF uses the spatial information for binary label inference, while SFCCRF uses the spatial information for soft-label inference. Consequently, the TGSFCRF model relies upon a mixture model that simultaneously describes the target and the background, which causes model limitations due to the fact that the background is often too complex to be modeled by one mode. In contrast, the adoption of numerous continuous states in SFCCRF to describe the background provides increased freedom to accommodate the heterogeneity and complexity of the background. Second, although both algorithms adopt the thresholding methods, TGSFCRF performs thresholding on the noisy original imagery with great class overlapping to obtain the unary statistics, while SFCCRF performs on the clean soft-label imagery with clearer class boundaries in the histogram domain to obtain binary labels. Therefore, the thresholding in SFCCRF is more robust than in the TGSFCRF algorithm. Third, SFCCRF is tailored to the noise characteristics of SAR image by addressing the multiplicative Gamma noise in the unary potential rather than using the Gaussian noise assumed by the TGSFCRF algorithm.

The enhanced total variation (ETV) model performs noise suppression before segmenting SAR imagery for sea ice mapping [22]. Both ETV and SFCCRF exploit the spatial correlation effect in SAR imagery to estimate the hidden states of the observed SAR imagery. Compared with ETV, SFCCRF has the following advantages. First, due to the stochastic cliques, SFCCRF tends to adopts only the most relevant pixels in the neighborhood, and as such SFCCRF is less sensitive to the outliers than ETV that adopts all the pixels in the neighborhood. Second, to describe the multiplicative SAR speckle noise, SFCCRF uses the Gamma distribution, which is more accurate than the Gaussian distribution in logarithmic domain that is adopted implicitly by ETV [32]. As a result, the associated probabilistic measures in SFCCRF are more robust to speckle noise, and more capable of reflecting the genuine similarity between SAR pixels.

The contribution of this paper lies in the following aspects. (i) A SFCCRF model is used for SAR image modeling and label inference, leading to an efficient SAR dark-spot detection algorithm. Since SFCCRF explains the generative characteristics of SAR image and accounts for the large-scale spatial correlation effect in SAR image, it can highlight the difference between the target and the background, and better discriminate weak targets. (ii) The statistical distribution of SAR speckle noise is addressed and built into the unary po-

tential and the data similarity likelihood, and as such SFCCRF addresses the particularities of SAR speckle noise and resists its influence. (iii) An effective optimization method based on gradient descent approach is designed for solving the SFCCRF model.

The rest of the paper is organized as follows. Section III describes the implementation and the optimization of SFCCRF, as well as the summary of the complete dark-spot detection algorithm. Section IV presents the experiment results on both simulated and real SAR images.

III. SFCCRF

A. Problem Formulation

We denote the discrete lattice spanned by SAR imagery by G and a site in the lattice by $i \in G$. We represent the intensity observation at site i by x_i, and the soft-label of site i by s_i. Then, a SAR image is expressed as $X = \{x_i | i \in G\}$ and the soft-labels of this image as $S = \{s_i | i \in G\}$. Pixel intensity values in X are linearly normalized into $[a, b]$ interval by using the equation:

$$x = \frac{(x - \min\{X\})(b - a)}{(\max\{X\} - \min\{X\})} + a \tag{1}$$

Moreover, the soft-labels in S share the same value range with X. Since s_i can take any decimal fraction values within $[a, b]$, rather than the integer values of either a or b, the resulting model is a CCRF model, rather than a discrete CRF model. Moreover, a low value of s_i indicates that x_i has high probability of being dark-spot, but low possibility of being the background. Due to these constraints, the soft-label s_i can be treated as the "true" backscattering intensity at site i for which a smaller value also indicates higher possibility of being the target. Considering the multiplicative nature of speckle noise, x_i can be expressed as a combination of the "true" backscattering state s_i and the noise state n_i:

$$x_i = s_i n_i \ (i = 1, 2, ..., N) \tag{2}$$

where N is the number of pixels in the image, and x_i satisfies a Gamma distribution [33]:

$$p(x_i | s_i) = \frac{1}{\Gamma(L)} \left(\frac{L}{s_i}\right)^L x_i^{L-1} e^{-L x_i / s_i} \tag{3}$$

where $\Gamma(\cdot)$ is the Gamma function, and L is the equivalent number of looks (ENL) of the SAR image X.

The task of dark-spot detection aims to infer S based on X, which is achieved here by a SFCCRF model, as described in Sections III-B and III-C. Based on S, a thresholding is performed to achieve the binary labels $Y = \{y_i | i \in G\}$, as described in Section III-D.

B. Model Specification

According to CCRF, the estimation of the soft-labels in S given X is achieved by maximizing the following posterior distribution:

$$p(S|X) = \frac{1}{Z(X)} exp\left\{\sum_i \psi_u(s_i, X) + \beta \sum_i \sum_{j \in N_i} \psi_p(s_i, s_j, X)\right\} \tag{4}$$

where $Z(X)$ is the partition function, ψ_u and ψ_p are respectively the unary potential and the pairwise potential, β determines the weight of the pairwise potential, and N_i is a collection the neighboring pixels around pixel i. Since only pixels in N_i are considered being connected with the referenced pixel i, N_i determines the pairwise clique structure in CRF. Based on the different implementations of N_i, we define the CCRF, the fully-connected CCRF (FCCRF) and the proposed SFCCRF from a comparative perspective.

- CCRF: N_i consists of all the pixels in a small neighborhood around pixel i, e.g., a 3×3 image patch centered at the ith pixel.
- FCCRF: N_i involves all the pixels in the whole image.
- SFCCRF: N_i involves a subset of pixels in the whole image, and the pixels in N_i are randomly selected from the whole imagery according to a stochastic clique approach.

We illustrate below the implementation of five key factors in SFCCRF, i.e., the stochastic clique, the unary potential $\psi_u(s_i, X)$, the pairwise potential $\psi_p(s_i, s_j, X)$, the data similarity likelihood P_{ij} and the spatial closeness measurement Q_{ij}.

1) Stochastic Clique: The stochastic clique approach selects the pixels in N_i from the image G according to a stochastic measure, i.e., $N_i = \{j | j \in G \ and \ I(i, j) = 1\}$, where,

$$I(i, j) = \begin{cases} 1, & \text{if } \gamma P_{ij} Q_{ij} \geqslant \varphi \\ 0, & \text{otherwise} \end{cases} \tag{5}$$

where P_{ij} measures the intensity similarity between pixels x_i and x_j, Q_{ij} measures the spatial closeness from x_i to x_j in image space, γ determines the sparsity of the graph, and φ is a random value in the range of $[0, 1]$ generated from an uniform distribution. Therefore, in the graphical model displayed by Fig. 1, the edge e_{ik} between s_i and s_k is determined based on the stochastic measure defined in (5), which favors close nodes for building connectivity with the referenced node s_i. By adopting the stochastic clique approach, SFCCRF is capable of utilizing the advantages of fully-connected graph, while reducing greatly the computational cost.

2) Unary Potential: The unary potential is implemented as follows:

$$\psi_u(s_i, X) = log(p(x_i | s_i)) \tag{6}$$

where $p(x_i|s_i)$ is defined in (3) to account for the multiplicative SAR speckle noise, and $log(p(x_i|s_i))$ has the following expression after removing constant terms:

$$log(p(x_i | s_i)) = L(log(x_i) - log(s_i) - x_i/s_i) - log(x_i) \tag{7}$$

The unary potential defined above promotes the consistency between the observation x_i and the soft-label s_i by yielding a bigger value for better matching between x_i and s_i.

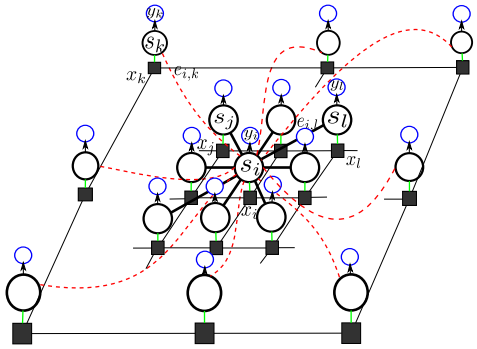

Fig. 1. The graphical structure of SFCCRF, where the three layers from bottom to top are respectively the observations layer, the soft-label layer and the binary label layer. In the middle layer, the edge e_{ik}, i.e., the connectivity between the referenced node s_i and an arbitrary node s_k, is determined by a stochastic measure, according to which, closer nodes have higher possibility (black solid edges) to be connected, whereas two nodes with larger distance are less likely to be connected (red dashed edges).

3) Pairwise Potential: The pairwise potential is expressed as follows:

$$\psi_p(s_i, s_j, X) = -\frac{(s_i - s_j)^2 P_{ij}}{\sum_{j \in N_i} P_{ij}} \tag{8}$$

This pairwise potential encourages pixel i to have similar label value with pixels in N_i. Moreover, s_i is more encouraged to be equal to s_j, if pixels i and j have larger data similarity P_{ij}.

4) Data Similarity Likelihood: Both the stochastic clique in (5) and the pairwise potential in (8) depend on P_{ij}, i.e., the intensity similarity likelihood between pixel x_i and x_j. Instead of calculating the similarity between two pixels at site i and j, we calculate the similarity between two image patches centered at pixel i and j, to resist the influence of noise and utilize the local information in image patches.

Based on the Gamma distribution in (3), the probabilistic similarity between two amplitude values $a_i = \sqrt{x_i}$ and $a_j = \sqrt{x_j}$ is expressed as [34]:

$$p(a_i, a_j) = 4L \frac{\Gamma(2L-1)}{\Gamma(L)} \left(\frac{a_i a_j}{a_i^2 + a_j^2} \right)^{2L-1} \tag{9}$$

Accordingly, the probabilistic similarity between two image patches centered at site i and j is the product of all pixels measures:

$$P_{ij} = \left(\prod_{k}^{K} p(a_{ik}, a_{jk}) \right)^{1/\tau} \tag{10}$$

where k is used to iterate through all corresponding pixels within the two patches, K is the total number of pixels in image patch, and τ is a scaling parameter.

5) Probabilistic Spatial Closeness Measurement: The stochastic clique in (5) relies on Q_{ij}, i.e., the probabilistic spatial closeness measurement between pixel x_i and x_j, which is defined as follows:

$$Q_{ij} = exp\left(-\frac{(J_{ir} - J_{jr})^2 + (J_{ic} - J_{jc})^2}{2\sigma^2} \right) \tag{11}$$

where J_{ir} and J_{ic} are respectively the row and column locations of site i in image space, and σ determines the spatial scale.

C. Model Optimization

Based on the model specifications in Sections III-B2 and III-B3, the objective function in (4) is reformulated as:

$$\begin{aligned} p(S|X) = \frac{1}{Z(X)} exp \Bigg\{ -\sum_i (L(log(s_i) \\ + x_i/s_i - log(x_i)) + log(x_i)) \\ -\beta \sum_i \sum_{j \in N_i} \frac{(s_i - s_j)^2 P_{ij}}{\sum_{j \in N_i} P_{ij}} \Bigg\} \end{aligned} \tag{12}$$

which has the following negative log-likelihood expression (12):

$$\begin{aligned} \mathfrak{L} = \sum_i (L(log(s_i) + x_i/s_i - log(x_i)) + log(x_i)) \\ +\beta \sum_i \sum_{j \in N_i} \frac{(s_i - s_j)^2 P_{ij}}{\sum_{j \in N_i} P_{ij}} \end{aligned} \tag{13}$$

The objective function in (13) is solved by gradient descent approach, which repeats until the estimation stabilizes the iterative update of s_i using the gradient.

$$\begin{aligned} &\text{repeat until the estimate stabilizes}\{ \\ &s_i := s_i - \alpha \frac{\partial \mathfrak{L}}{\partial s_i}, \ for \ i = 1, 2, ..., N \\ &\} \end{aligned} \tag{14}$$

where α is the learning rate, and,

$$\frac{\partial \mathfrak{L}}{\partial s_i} = -L \left(\frac{x_i - s_i}{s_i^2} \right) - 2\beta(v_i - s_i) \tag{15}$$

where

$$v_i = \frac{\sum_{j \in N_i} s_j P_{ij}}{\sum_{j \in N_i} P_{ij}} \tag{16}$$

The presence of L in (15) allows adjusting the weight of data consistency according to the noise levels. Higher noise level causes smaller L value, thereby decreased importance of data consistency.

Since (15) does not allow s_i to be zero, in (1), we normalize x into interval $[1, 2]$, rather than $[0, 1]$ to prevent the case when $s_i = 0$.

D. Summary of Complete Algorithm

The final step is to perform a thresholding on the soft-label S to get the binary label Y, according to the following rule:

$$y_i = \begin{cases} 0, \ if \ s_i < thrd \\ 1, \ if \ s_i \geqslant thrd \end{cases} \tag{17}$$

where $thrd = mean(S) - \varepsilon \cdot std(S)$, with ε usually being 1.

The complete dark-spot detection algorithm is summarized in Algorithm 1.

Algorithm 1 SFCCRF

Input: SAR image X
Output: binary label Y
Initialization: Normalize X into $[1, 2]$, $S = X$

1: **while** $iter < TotalIters$ **do**
2: **for** $i = 1, 2, ..., N$ **do**
3: **for** $j = 1, 2, ..., N$ **do**
4: calculate P_{ij} and Q_{ij} by (10) and (11) respectively
5: include j into N_i, if $I(i, j) = 1$ in (5)
6: **end for**
7: calculate v_i according to (16)
8: **end for**
9: $R = -L((X - S)/S^2) - 2\beta(V - S)$ according to (15)
10: $S = S - \alpha R$ according to (14)
11: **end while**
12: obtain Y according to (17)

IV. Experiments and Discussion

In this section, we start with the introduction to the experimental setup, followed by the discussion of the results achieved by different approaches on both simulated and real SAR images.

A. Experimental Setup

We test SFCCRF on both simulated and real SAR images, in comparison with several other approaches. The performance is evaluated using several numerical measures.

1) Methods Compared: It is important to examine the performance differences among CCRF, FCCRF and SFCCRF, in the context of SAR dark-spot detection. The implementations of CRF, FCCRF, and SFCCRF are described below.

- CCRF is implemented by following Algorithm 1, but changing lines 3-6 in Algorithm 1 to achieve local connectivity. So, N_i includes all pixels in a 3×3 image patch.
- FCCRF is the same with CCRF except that N_i is set to include all pixels in a 21×21 image patch. Since N_i is fairly large, empirically, it can be used to represent the whole image. We found that using larger N_i causes increased computational cost, but decreased performance.
- SFCCRF is implemented by following Algorithm 1.

Moreover, we also compare the proposed method with one recent SAR noise-suppression approach, i.e., the enhanced total variation (ETV) method which has been used for SAR sea ice segmentation [22].

2) Parameter Setting: For all methods, we manually determine the model parameters using about 20% of the real SAR images, and use this parameter setting for testing on the simulated and the remaining real SAR images. For SFCCRF, we set $\gamma = 0.3$, $\tau = 1$, $\beta = 3$, $\sigma = 5$, $K = 9$, $\alpha = 0.95$, and $TotalIters = 20$. CCRF and FCCRF use the same parameter setting with SFCCRF when applicable. The parameter L of all methods is set according to the ENL of SAR imagery. In the simulated study, the value of ENL is pre-known because the speckle noise with known ENL values is generated to simulate the SAR images. For real SAR images, the nominal ENL value is 4 for the product of RADARSAT-1 ScanSAR Narrow Mode.

3) Numerical Measures: We use three statistics, i.e., omission error (OE), commission error (CE), and averaged error (AE), to measure the inconsistency between the detected target and the ground-truth target [35].

Let A_E and A_R denote respectively the size of detected target and the size of ground-truth target. Then CE is expressed as:

$$CE = \frac{A_E - A_{EinR}}{A_E} \tag{18}$$

where A_{EinR} is the size of the overlapping area between the detected target and the ground-truth target. Therefore, CE reflects the proportion of the false detections in all detections. Conversely, the OE is expressed as:

$$OE = \frac{A_R - A_{RinE}}{A_R} \tag{19}$$

where A_{RinE} is the size of ground-truth target within a certain distance of the detected target. So, OE indicates the ratio of the omissions in detection relative to the ground-truth target. By combining CE and OE, AE provides a balanced evaluation of the detection capability:

$$AE = \frac{CE + OE}{2} \tag{20}$$

The above-defined statistics are used to evaluate the performance of different algorithms on both simulated and real SAR images.

B. Experiments With Simulated SAR Images

To test the algorithms under a controlled environment, SAR images are simulated by degrading a 128×128 sized clean image (as shown in Fig. 2) with speckle noise. The speckle noise follows a Gamma distribution, as formulated in (3), and the noise level is determined by L. A total of eleven SAR images with different noise levels are simulated by setting $L = 1, 2, ..., 11$. Different methods are tested on these eleven images. In addition to ETV, CCRF, FCCRF and SFCCRF, in this simulated study, we adopt an intensity thresholding method, called "IThrhd", where the threshold equals mean intensity minus one standard deviation.

Fig. 2. The clean image used for simulating SAR images.

Fig. 3 displays the OE, CE and AE achieved by different methods on images of different noise levels. SFCCRF outperforms ETV, CCRF and FCCRF according to all measures

on most noise levels. FCCRF achieves lower AE and OE than CCRF in most cases, especially when the noise level is high. ETV achieves lower CE values than CCRF and FCCRF. All CRF-based methods perform much better than the IThrhd approach.

Fig. 4 shows the detection results achieved by different methods on three simulated images of different noise levels, i.e., L=2, L=7 and L=11. CCRF performs much better than the IThrhd approach, which tends to produce very high detection error. But CCRF still has many false detection and omissions. FCCRF achieves fewer omissions, but tends to inflate the targets. ETV achieves better results than FCCRF. SFCCRF achieves a good balance between omission and commission error.

Fig. 5 shows the noisy image and the soft-labels of this image inferred by SFCCRF, as well as their histograms. As we can see, SFCCRF can enhance the contrast between dark-spots and background. In histogram domain, the modality that once hidden in Fig. 5c is revealed in Fig. 5d.

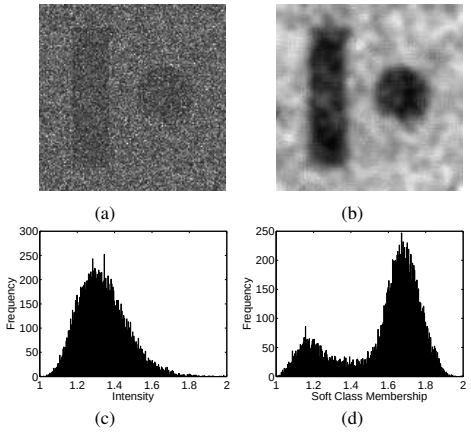

Fig. 5. (a) Noisy image with L=10. (b) The soft-label(s) inferred by SFCCRF. (c) The histogram of the noisy image. (d) The histogram of soft-labels.

Fig. 6 shows the receive operating characteristic (ROC) curves of different methods when $L = 2$. Overall, the curve of SFCCRF is above the curves of all others, indicating that the soft-labels produced by SFCCRF have the strongest discriminative capability. ETV is very close to SFCCRF and seems to be the second best. FCCRF outperforms CCRF in most cases. All CRF-based methods perform better than IThrhd.

C. Experiments With Real SAR Images

A total of 22 RADARSAT-1 ScanSAR intensity images of different image sizes, with HH polarization and spatial resolution of 50×50 meters, provided by Canadian Ice Service (CIS) from the oil-spill target database of ISTOP [36], are used for testing the algorithms. Each image contains at least one anomaly, and the 22 image dataset covers the major types of anomalies detected by human analysts in CIS under a variety of sea conditions.

The algorithms are tested on all the images, and the statistics of the numerical measures achieved by different methods are summarized in Table I. The results are generally consistent

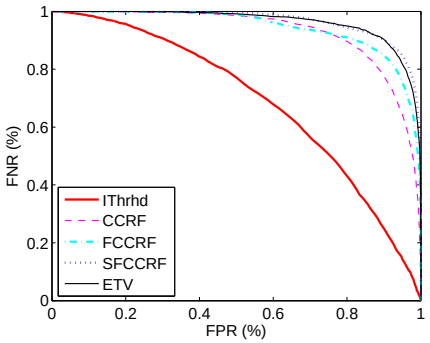

Fig. 6. The ROC curves of different methods, showing the trade-off between false positive rate (FPR) and false negative rate (FNR) as the decision threshold varies. In ROC, higher closeness of the curve to the top and right axes implies higher discriminative capability of the associated method. Accordingly, the proposed SFCCRF method indicates the strongest discriminative capability. ETV is very close to SFCCRF.

with the simulated study. SFCCRF achieves much lower AE and CE than the other methods. ETV ranks the second best in terms of the mean statistics of all measures. In terms of AE, FCCRF outperforms CCRF, which, although yields low OE, produces very high CE. All CRF-based methods obtain lower errors than the IThrhd approach.

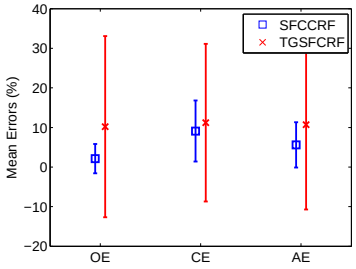

Fig. 7. The comparison of error statistics achieved by the proposed SFCCRF method and the error statistics achieved by TGSFCRF reported in [29] on the same SAR images.

Fig. 8 shows the detection results achieved by different methods on four images. CCRF tends to break the elongated targets, and wrongly detect dark pixels in the background as targets. FCCRF is less affected by the background heterogeneity than CCRF. But FCCRF tends to expand the boundaries. ETV performs better than FCCRF, but still tends to inflate the target and erase some thin targets. SFCCRF can accurately identify the targets, without being affected too much by the background and target heterogeneities.

Fig. 7 shows the comparison of error statistics achieved by the proposed SFCCRF method and the error statistics achieved by TGSFCRF reported in [29] on the same SAR images. As we can see, SFCCRF achieved lower mean errors with smaller standard deviations.

All algorithms were implemented under the MATLAB platform. On average, it took 31.7, 9.3, 78.4, and 34.1 seconds, respectively, for ETV, CCRF, FCCRF, and SFCCRF to process a 512-by-512 sized SAR image using a Pentium 3.40-GHZ Quad-Core processor.

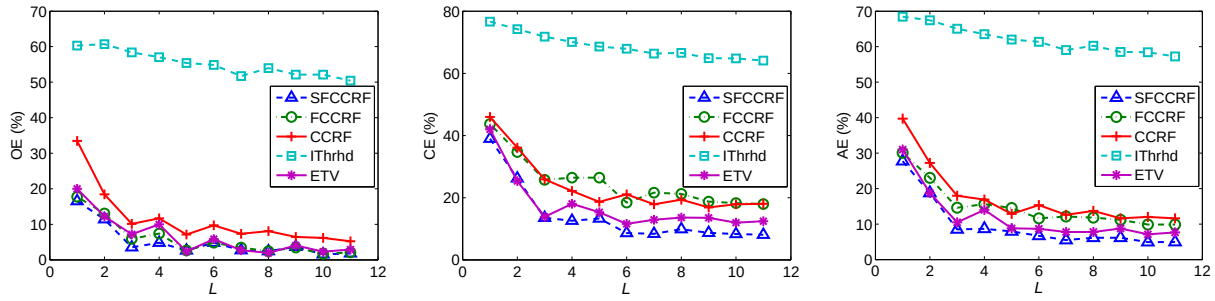

(a) (b) (c)

Fig. 3. The plots of OE (a), CE (b) and AE (c) achieved by different methods over various noise levels measured by ENL, which is denoted by L. In all plots, lower statistic values indicate better results. The proposed SFCCRF method achieves the lowest error lines on CE and AE, and slightly lower line on OE, indicating the highest performance according to all measures.

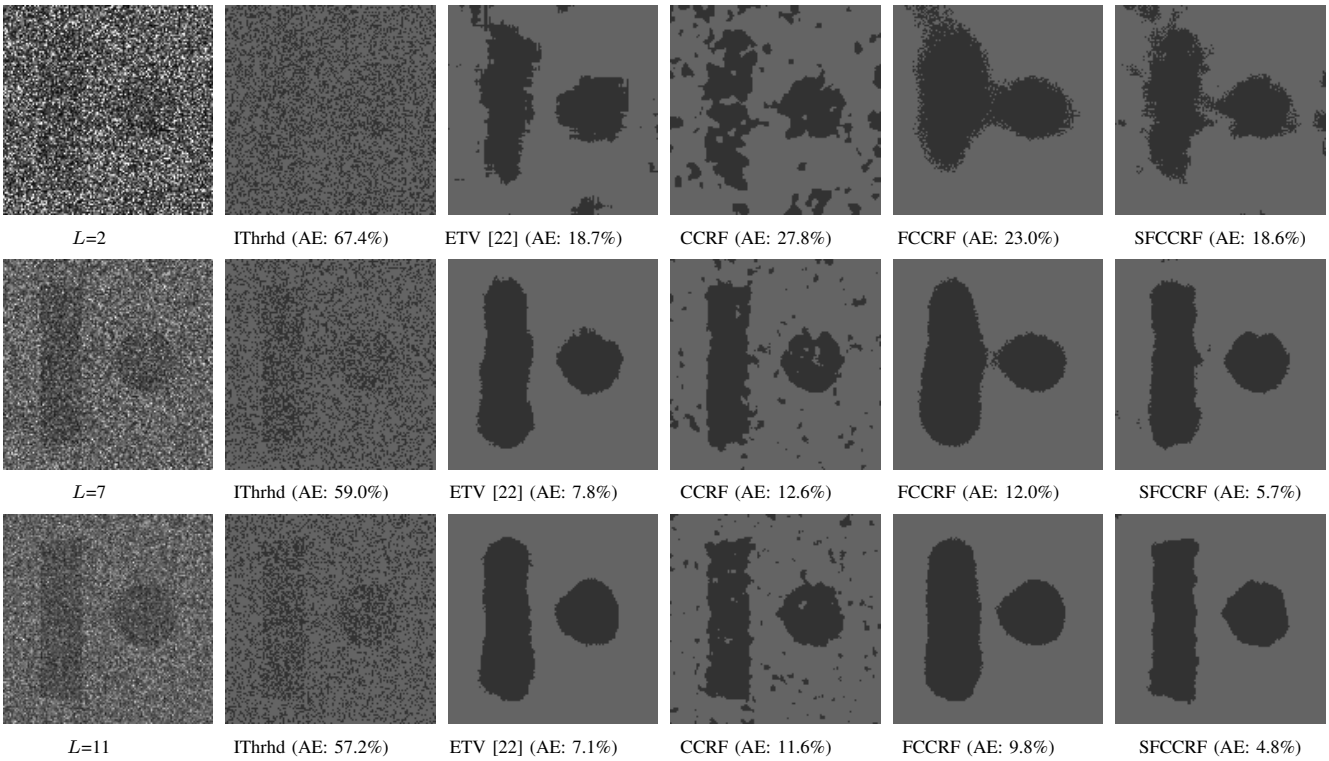

Fig. 4. The detection results achieved by different methods on three simulated images of different noise levels, i.e., L=2, L=7 and L=11. The AE values are included. In general, the proposed SFCCRF method can better delineate the boundary without being seriously influenced by the noise effect.

TABLE I

STATISTICS (I.E., MEAN, STANDARD DEVIATION) OF OMISSION ERROR (OE), COMMISSION ERROR (CA) AND AVERAGED ERROR (CA) ACHIEVED BY DIFFERENT METHODS ON REAL SAR IMAGES. FOR ALL STATISTICS, LOWER VALUES INDICATE BETTER PERFORMANCE.

	OE		CE		AE	
	Mean (%)	Std. (%)	Mean (%)	Std. (%)	Mean (%)	Std. (%)
SFCCRF	2.1	3.7	**9.1**	**7.7**	**5.6**	**5.7**
CCRF	**0.3**	**0.6**	23.7	16.6	12.0	8.6
FCCRF	5.5	7.8	16.2	13.1	10.8	10.4
ETV	3.7	5.7	13.4	11.5	8.5	8.6
IThrhd	25.7	11.2	82.0	10.4	53.9	10.8

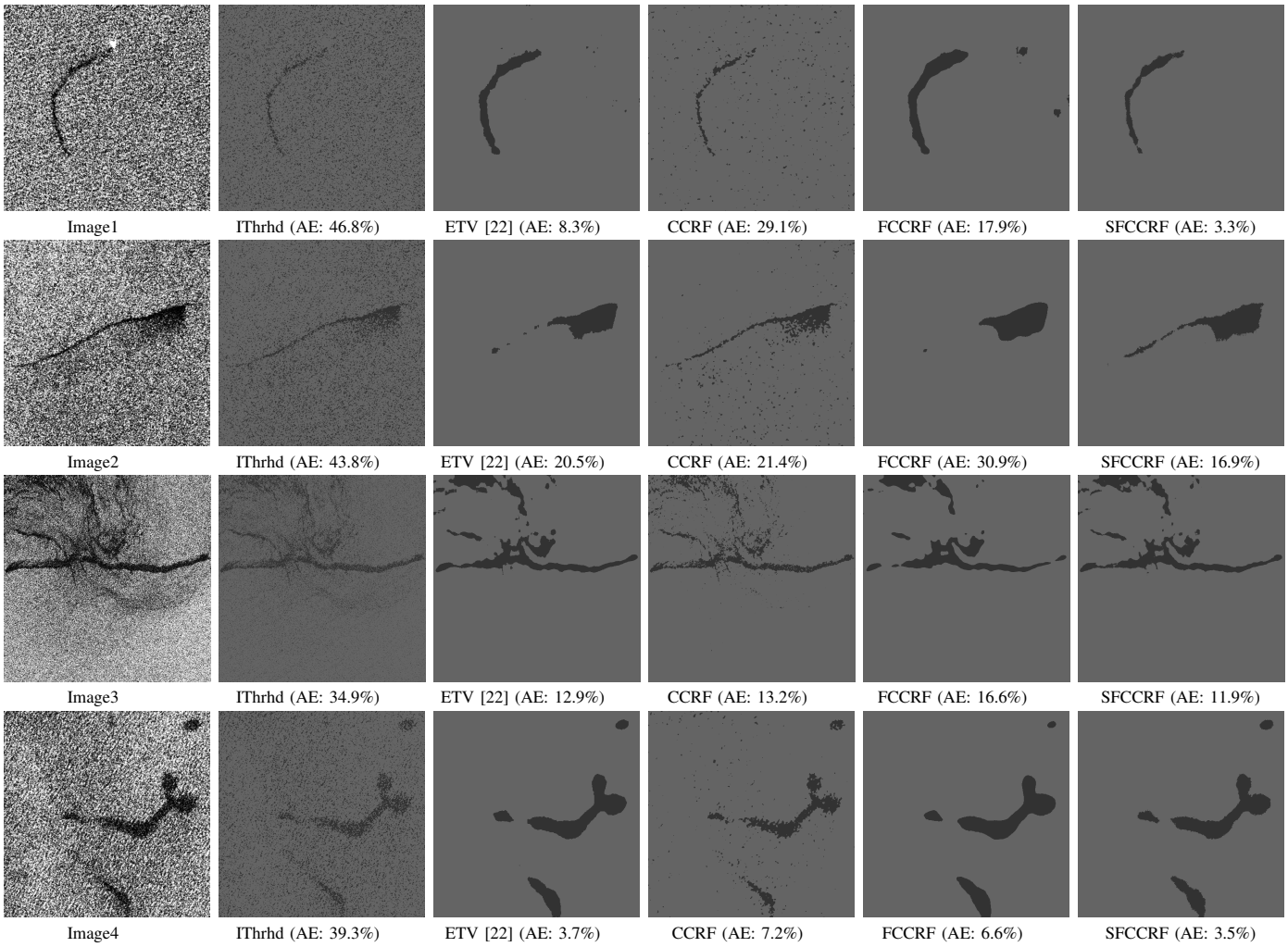

Fig. 8. The detection results achieved by different methods on four images. The results are generally consistent with Fig. 4. Comparing with the other methods, the proposed SFCCRF method is less affected by the background and target heterogeneities, and in the meantime can more accurately identify the boundaries and the linear targets.

V. Conclusions

In this paper, we presented a SFCCRF approach to model SAR image and to perform soft-label inference, leading to an efficient dark-spot detection algorithm. In SFCCRF, we adopted a stochastic measure to determine the graph connectivity among pixels, providing an efficient way to model global-scale spatial correlation effect in SAR imagery. We built the statistical distribution of SAR speckle noise into the unary potential and the data similarity likelihood to accommodate the particularities of SAR images. We derived an effective optimization method based on gradient descent approach. Given the soft-labels inferred by SFCCRF, a binarization is performed to achieve the task of dark-spot detection. The experiments on both simulated and real SAR images demonstrate the robustness of the proposed SFCCRF against speckle noise, and its accuracy in detecting dark-spots in SAR imagery under intense background heterogeneity.

VI. Acknowledgements

This work is partly funded by the Natural Sciences and Engineering Research Council of Canada (NSERC) and the Canadian Space Agency (CSA). This research was undertaken, in part, thanks to funding from the Canada Research Chairs program.

References

[1] F. Wiese, "Seabirds and Atlantic Canada's ship-source oil pollution: Impacts, trends, and solutions," *World Wildlife Fund Canada Contract Report*, 2002.

[2] A. Cheng, M. Arkett, T. Zagon, R. De Abreu, D. Mueller, P. Vachon, and J. Wolfe, "Oil detection in RADARSAT-2 quad-polarization imagery: implications for ScanSAR performance," in *SPIE Remote Sensing*. International Society for Optics and Photonics, 2011, pp. 81 790G–81 790G.

[3] K. N. Topouzelis, "Oil spill detection by SAR images: dark formation detection, feature extraction and classification algorithms," *Sensors*, vol. 8, no. 10, pp. 6642–6659, 2008.

[4] M. Fingas and C. Brown, "Review of oil spill remote sensing," *Marine pollution bulletin*, vol. 83, no. 1, pp. 9–23, 2014.

[5] W. Alpers and H. Hühnerfuss, "The damping of ocean waves by surface films: A new look at an old problem," *Journal of Geophysical Research: Oceans (1978–2012)*, vol. 94, no. C5, pp. 6251–6265, 1989.

[6] W. Alpers, V. Wismann, R. Theis, H. Huhnerfuss, N. Bartsch, J. Moreira, and J. Lyden, "The damping of ocean surface waves by monomolecular sea slicks measured by airborne multi-frequency radars during the SAXON-FPN experiment," in *Geoscience and Remote Sensing Symposium, 1991. IGARSS'91. Remote Sensing: Global Monitoring for Earth Management., International*, vol. 4. IEEE, 1991, pp. 1987–1990.

[7] H. A. Hovland, J. A. Johannessen, and G. Digranes, "Slick detection in SAR images," in *Geoscience and Remote Sensing Symposium, 1994. IGARSS'94. Surface and Atmospheric Remote Sensing: Technologies, Data Analysis and Interpretation., International*, vol. 4. IEEE, 1994, pp. 2038–2040.

[8] C. Brekke and A. H. Solberg, "Oil spill detection by satellite remote sensing," *Remote sensing of environment*, vol. 95, no. 1, pp. 1–13, 2005.

[9] Y. Shu, J. Li, H. Yousif, and G. Gomes, "Dark-spot detection from SAR intensity imagery with spatial density thresholding for oil-spill monitoring," *Remote Sensing of Environment*, vol. 114, no. 9, pp. 2026–2035, 2010.

[10] F. Nirchio, M. Sorgente, A. Giancaspro, W. Biamino, E. Parisato, R. Ravera, and P. Trivero, "Automatic detection of oil spills from SAR images," *International Journal of Remote Sensing*, vol. 26, no. 6, pp. 1157–1174, 2005.

[11] B. Fiscella, A. Giancaspro, F. Nirchio, P. Pavese, and P. Trivero, "Oil spill detection using marine SAR images," *International Journal of Remote Sensing*, vol. 21, no. 18, pp. 3561–3566, 2000.

[12] A. S. Solberg, G. Storvik, R. Solberg, and E. Volden, "Automatic detection of oil spills in ERS SAR images," *Geoscience and Remote Sensing, IEEE Transactions on*, vol. 37, no. 4, pp. 1916–1924, 1999.

[13] A. H. Solberg, S. T. Dokken, and R. Solberg, "Automatic detection of oil spills in Envisat, Radarsat and ERS SAR images," in *Geoscience and Remote Sensing Symposium, 2003. IGARSS'03. Proceedings. 2003 IEEE International*, vol. 4. IEEE, 2003, pp. 2747–2749.

[14] A. H. S. Solberg, C. Brekke, and P. Ove Husoy, "Oil spill detection in Radarsat and Envisat SAR images," *Geoscience and Remote Sensing, IEEE Transactions on*, vol. 45, no. 3, pp. 746–755, 2007.

[15] C. Chen, K. Chen, L. Chang, and A. Chen, "The use of satellite imagery for monitoring coastal environment in Taiwan," in *Geoscience and Remote Sensing, 1997. IGARSS'97. Remote Sensing-A Scientific Vision for Sustainable Development., 1997 IEEE International*, vol. 3. IEEE, 1997, pp. 1424–1426.

[16] A. K. Liu, C. Y. Peng, and S.-S. Chang, "Wavelet analysis of satellite images for coastal watch," *Oceanic Engineering, IEEE Journal of*, vol. 22, no. 1, pp. 9–17, 1997.

[17] S. Wu and A. Liu, "Towards an automated ocean feature detection, extraction and classification scheme for SAR imagery," *International Journal of Remote Sensing*, vol. 24, no. 5, pp. 935–951, 2003.

[18] S. Derrode and G. Mercier, "Unsupervised multiscale oil slick segmentation from SAR images using a vector HMC model," *Pattern Recognition*, vol. 40, no. 3, pp. 1135–1147, 2007.

[19] K. Topouzelis, V. Karathanassi, P. Pavlakis, and D. Rokos, "Detection and discrimination between oil spills and look-alike phenomena through neural networks," *ISPRS Journal of Photogrammetry and Remote Sensing*, vol. 62, no. 4, pp. 264–270, 2007.

[20] A. Taravat and N. Oppelt, "Adaptive weibull multiplicative model and multilayer perceptron neural networks for dark-spot detection from sar imagery," *Sensors*, vol. 14, no. 12, pp. 22 798–22 810, 2014.

[21] Y. Li and J. Li, "Oil spill detection from SAR intensity imagery using a marked point process," *Remote Sensing of Environment*, vol. 114, no. 7, pp. 1590–1601, 2010.

[22] T.-J. Kwon, J. Li, and A. Wong, "Etvos: An enhanced total variation optimization segmentation approach for sar sea-ice image segmentation," *Geoscience and Remote Sensing, IEEE Transactions on*, vol. 51, no. 2, pp. 925–934, 2013.

[23] J.-S. Lee, "Digital image enhancement and noise filtering by use of local statistics," *Pattern Analysis and Machine Intelligence, IEEE Transactions on*, no. 2, pp. 165–168, 1980.

[24] V. S. Frost, J. A. Stiles, K. S. Shanmugan, and J. C. Holtzman, "A model for radar images and its application to adaptive digital filtering of multiplicative noise," *Pattern Analysis and Machine Intelligence, IEEE Transactions on*, no. 2, pp. 157–166, 1982.

[25] D. T. Kuan, A. Sawchuk, T. C. Strand, P. Chavel *et al.*, "Adaptive noise smoothing filter for images with signal-dependent noise," *Pattern Analysis and Machine Intelligence, IEEE Transactions on*, no. 2, pp. 165–177, 1985.

[26] J. Lafferty, A. McCallum, and F. C. Pereira, "Conditional random fields: Probabilistic models for segmenting and labeling sequence data," *in Proceedings of ICML*, pp. 282–289, 2001.

[27] C. Sutton and A. McCallum, "An introduction to conditional random fields," *Machine Learning*, vol. 4, no. 4, pp. 267–373, 2011.

[28] M. Shafiee, A. Wong, P. Siva, and P. Fieguth, "Efficient Bayesian inference using fully connected conditional random fields with stochastic cliques," in *International Conference on Image Processing (ICIP). IEEE*, 2014, pp. 1–5.

[29] L. Xu, M. J. Shafiee, A. Wong, F. Li, L. Wang, and D. Clausi, "Oil spill candidate detection from SAR imagery using a thresholding-guided stochastic fully-connected conditional random field model," in *Computer Vision and Pattern Recognition (CVPR) EARTHVISION Workshop, 2015 IEEE Conference on*, 2015, pp. 79–86.

[30] T. Qin, T.-Y. Liu, X.-D. Zhang, D.-S. Wang, and H. Li, "Global ranking using continuous conditional random fields," in *Advances in neural information processing systems*, 2009, pp. 1281–1288.

[31] V. Radosavljevic, S. Vucetic, and Z. Obradovic, "Continuous conditional random fields for regression in remote sensing." in *ECAI*, 2010, pp. 809–814.

[32] H. Xie, L. E. Pierce, and F. T. Ulaby, "Statistical properties of logarithmically transformed speckle," *Geoscience and Remote Sensing, IEEE Transactions on*, vol. 40, no. 3, pp. 721–727, 2002.

[33] M. Dai, C. Peng, A. K. Chan, and D. Loguinov, "Bayesian wavelet shrinkage with edge detection for SAR image despeckling," *Geoscience and Remote Sensing, IEEE Transactions on*, vol. 42, no. 8, pp. 1642–1648, 2004.

[34] C.-A. Deledalle, L. Denis, and F. Tupin, "Iterative weighted maximum likelihood denoising with probabilistic patch-based weights," *Image Processing, IEEE Transactions on*, vol. 18, no. 12, pp. 2661–2672, 2009.

[35] C. Wiedemann, C. Heipke, H. Mayer, and O. Jamet, "Empirical evaluation of automatically extracted road axes," *Empirical Evaluation Techniques in Computer Vision*, pp. 172–187, 1998.

[36] M.-F. Gauthier, L. Weir, Z. Ou, M. Arkett, and R. De Abreu, "Integrated satellite tracking of pollution: A new operational program," in *Geoscience and Remote Sensing Symposium, 2007. IGARSS 2007. IEEE International*. IEEE, 2007, pp. 967–970.

Linlin Xu (M14) received his B.Eng. and M.Sc. degrees in geomatics engineering from China University of Geosciences, Beijing, China, in 2007 and 2010, respectively. He obtained his Ph.D. degree in geography from the University of Waterloo, Waterloo, ON, Canada. He is now working as a post-doc fellow in Vision and Image Processing Lab, Systems Design Engineering from the University of Waterlo. His current research interests are in the areas of hyperspectral and SAR image processing.

Mohammad Javad Shafiee received the B.Sc. and M.Sc. degrees in computer science and artificial intelligence from Shiraz University, Shiraz, Iran, in 2008 and 2011, respectively. He is currently pursuing the Ph.D. degree with the Department of Systems Design Engineering, University of Waterloo, Waterloo, ON, Canada. His research interests include computer vision, machine learning, and biomedical image processing. His main focus is on statistical learning and graphical models, such as conditional random fields and Markov random fields and deep learning.

Alexander Wong (M05) received the B.A.Sc. degree in computer engineering, the M.A.Sc. degree in electrical and computer engineering, and the Ph.D. degree in systems design engineering from the University of Waterloo, Waterloo, ON, Canada, in 2005, 2007, and 2010, respectively. He is currently an Assistant Professor with the Department of Systems Design Engineering, University of Waterloo. He has authored refereed journal and conference papers, as well as patents, in various fields, such as computer vision, graphics, image processing, multimedia systems, and wireless communications. His current research interests include image processing, computer vision, pattern recognition, and cognitive radio networks, with a focus on biomedical and remote sensing image processing and analysis such as image registration, image denoising and reconstruction, image super-resolution, image segmentation, tracking, and image and video coding and transmission. Dr. Wong was the recipient of an Outstanding Performance Award, an Engineering Research Excellence Award, an Early Researcher Award from the Ministry of Economic Development and Innovation, a Best Paper Award by the Canadian Image Processing and Pattern Recognition Society, and the Alumni Gold Medal.

David Clausi (S93M96SM03) received the BASc, MASc, and PhD degrees in systems design engineering from the University of Waterloo, Canada, in 1990, 1992, and 1996, respectively. After completing his PhD, he worked in the medical imaging field at Mitra Imaging Inc., Waterloo. He started his academic career as an assistant professor in geomatics engineering at the University of Calgary, Canada, in 1997. He returned to his alma mater in 1999 and was awarded tenure and promotion to associate professor in 2003. He is an active interdisciplinary and multidisciplinary researcher. He has an extensive publication record, publishing refereed journal and conference papers on remote sensing, computer vision, algorithm design, and biomechanics. His primary research interest is the automated interpretation of synthetic aperture radar (SAR) sea ice imagery, in support of operational activities of the Canadian Ice Service. The research results have led to successful commercial implementations. He has received numerous scholarships, conference paper awards, and two Teaching Excellence Awards. He is a senior member of the IEEE.